Optimization of Single-mode Sapphire Waveguide Bragg Gratings

Mohan Wang, Patrick S. Salter, Frank P. Payne, Tongyu Liu, Adrian Shipley, Zipei Song, Stephen M. Morris, Martin J. Booth, and Julian A. J. Fells

***Abstract*—We demonstrate the fabrication and optimization of waveguide Bragg gratings on single-crystal sapphire substrates using femtosecond laser direct writing. The gratings are fabricated using modulated bursts and are embedded inside single-mode depressed cladding waveguides. Through design optimization, and fabrication parameter tuning, a depressed cladding waveguide with a loss of ~0.8 dB/cm and a Bragg grating with a reflectivity of higher than 90% in the telecommunications wavelength band are demonstrated. The waveguide Bragg grating exhibits stable thermal properties under annealing at 1000°C. A sampled grating and a grating array are also demonstrated, showing the potential for more complex grating designs.**

***Index Terms*—Bragg gratings, femtosecond laser, integrated optics, micromachining, optical waveguides.**

I. Introduction

A waveguide Bragg grating (WBG) contains a periodic modulation in the effective refractive index, n_{eff}, along the waveguide. This grating reflects light at a Bragg wavelength, λ_B, according to

$$\lambda_B = 2n_{eff}\Lambda/m \quad (1)$$

where Λ is the pitch of the index modulation and m is the grating order [1]. Bragg gratings have a wide range of applications such as dispersion compensators for telecommunications [2], sensors for industrial or biomedical monitoring [3], and as cavity mirrors for lasers [4]. Femtosecond laser direct writing has become an established technology for the fabrication of Bragg gratings in substrates that are transparent to the laser wavelength. Through nonlinear interactions between the laser and material, permanent refractive index modification can be created to form three-dimensional structures at the laser focus.

Bragg gratings fabricated using the femtosecond laser point-by-point writing method were reported in 2004, by Martinez *et al*. [5]. The grating was demonstrated on a standard fiber, enabling flexible inscription without the need for photosensitization nor a phase mask. A femtosecond laser-written WBG manufactured using individual pulses of light to form the grating was reported in 2006 by Marshall *et al*. [6] on a glass substrate. Since then, many different femtosecond laser Bragg grating writing techniques have been developed on a wide range of materials including glass [7], polymer [8], and crystals [9].

Sapphire, or α-Al_2O_3, has attracted much research attention as an integrated photonics platform. Sapphire has a wide transmission bandwidth which extends to the mid-infrared, making it ideal for use in astrophysics and biomedicine. Moreover, the high melting point of 2050°C, as well as the chemical inertness and radiation resistance also allows robust operation under ultra-extreme environments. It has been widely used in industrial sensors [10], [11], [12], endoscope windows [13], and semiconductor substrates [14], with potential applications in display screens [15].

The most common type of Bragg grating in sapphire is inscribed within a sapphire fiber, utilizing a commercially available sapphire fiber as a waveguide. To this end, a femtosecond laser-written fiber Bragg grating was reported by Mihailov *et al*. using the phase-mask method within a 150-μm diameter sapphire fiber [16]. Subsequently, continuous research efforts have been undertaken to fabricate femtosecond laser-written multimode Bragg gratings in sapphire fiber using interferometry [16], [17], as well as point-by-point [18] and line-by-line [19] laser direct writing techniques. However, a sapphire fiber behaves as a multimode waveguide with tens of thousands of modes. Such an approach leads to very limited control over the Bragg grating mode performance. The shape of the sapphire fiber also confines the possible applications.

One solution to optimize the spectral response of the sapphire WBG is to tailor the waveguide design for a reduced number of modes. If a Bragg grating can be written within a single-mode waveguide, the spectral performance of the grating will be optimum. So far, most research has been focused on the lasing crystal Ti^{3+}-doped sapphire, where four different types of waveguide designs: single-track [20], dual-track [20], [21], depressed cladding [22], and micro-structured [23] waveguides have been demonstrated. These waveguides all exhibit few-mode behavior. The propagation loss, though measured under different wavelengths, is several dB/cm.

Meanwhile, there have been limited reports on waveguides or Bragg gratings in single-crystal planar sapphire substrates until recently. For example, Berubé *et al*. in 2019 reported a

This work was supported by the Engineering and Physical Sciences Research Council (EP/T00326X/1). *(Corresponding author: Julian A. J. Fells).*

Mohan Wang, Patrick S. Salter, Frank P. Payne, Tongyu Liu, Zipei Song, Stephen M. Morris, Martin J. Booth, and Julian A. J. Fells are with the Department of Engineering Science, University of Oxford, Parks Road, Oxford, OX1 3PJ, UK (e-mail: julian.fells@eng.ox.ac.uk).

Adrian Shipley is with the Rolls-Royce Plc, Derwent Building, 5000 Solihull Parkway, Birmingham Business Park, Birmingham, B37 7YP, UK.

depressed cladding waveguide (DCW) on single-crystal sapphire at mid-infrared wavelengths [24]. The laser modification area was fine-tuned to create a cladding geometry that supports single-mode guiding with a loss of < 0.37 dB/cm. It is more desirable to operate at shorter wavelengths, such as the telecommunications C band around 1550 nm where components are lower cost, but this requires higher precision fabrication as the dimensions scale with wavelength. By utilizing similar techniques to fabricate a DCW but targeting the near-infrared red wavelength band, we demonstrated single-mode DCWs and WBGs in both planar a sapphire substrate and sapphire fiber [25]. The WBGs had a narrow bandwidth of < 0.5 nm, with approximately 2 dB/cm waveguide loss, with a reflectivity of approximately 20%. Subsequently, Kefer *et al.* demonstrated a micro-structured waveguide and WBG in sapphire with a propagation loss of ~1 dB/cm. In this demonstration, the sample had a significant polarization splitting of 7 nm as the grating was not written along the optical axis. The asymmetric shape of the microstructure can also create polarization dependent behavior [26].

In this paper, we present an optimized design process for WBGs fabricated using modulated bursts within single-mode DCWs, with low propagation loss, high reflectivity, and low polarization dependence. The structure of the paper is organized as follows. Part II presents the fabrication and optimization of the DCW in which the gratings are to be embedded. Part III presents the inscription and characterization of a Bragg grating. Part IV presents the thermal stability of the WBG. A discussion on how the grating spectral performance could be further optimized is provided in Part V, followed by the demonstration of a sampled grating and a multiplexed grating array in Part VI.

II. Fabrication and Optimization of the Depressed Cladding Waveguide

A. Waveguide Design and Fabrication

A regeneratively amplified femtosecond laser system (Light Conversion, Pharos SP-06-1000-PP) was used for fabrication, delivering a second harmonic generation wavelength of 515 nm with a pulse duration of 170 fs, and a repetition rate of 1 MHz. The pulse energy was adjusted using a half-waveplate and a polarizer. The output laser beam was expanded using a telescope and projected onto a liquid crystal phase-only spatial light modulator (SLM, Hamamatsu X10468). A pre-aberrated wavefront was displayed on the SLM to compensate for the refractive index mismatch between the sapphire sample ($n_{sapphire}$ = 1.773 at 515 nm) and air [27]. The SLM phase image was then projected onto the back pupil plane of a ×40, 0.75 NA objective (Zeiss EC Plan-Neofluar 40×, 0.75) using a 4-*f* imaging system.

Two different sizes of sapphire substrates with dimensions of 10×10×1.2 mm and 40×10×1.2 mm (PI-KEM) were used. The optical axis, *c*-axis, is in plane with the main face, which is the *M*-plane [$(01\bar{1}0)$]. The substrates were mounted on a three-dimensional nano-precision motion stage (Aerotech ABL10100L for *x* and *y* axes and ANT95-3-V for the *z* axis). The laser polarization direction was perpendicular to the optical axis of the sapphire crystal. We define a track as a line of negative refractive index change throughout the substrate, fabricated by horizontally translating the sapphire substrate against the laser focus. Tracks were inscribed at a depth of 400 μm below the surface at a translation speed of 11 mm/s. Crack mitigation was achieved by tuning the laser pulse energy and track geometry through an iterative adjustment process. The optimum pulse energy was found to be 28 nJ. After fabrication, the laser-modified area was examined under an optical microscope and the dimensions were recorded.

The DCW was designed using the laser-modification track geometry following the approach described in our previous work [25]. For a waveguide with finite cladding size, the radiation loss is the dominant propagation loss, which can be optimized by increasing the cladding-to-core ratio [28]. For this reason, extra layers were added in the horizontal direction to make the waveguide shape circular as the tracks were elliptical in shape (~5 × 3 μm for height and width). A Similar design has been reported by Okhrimchuk *et al*. on a YAG:Nd crystal [29] and Nyguyen *et al*. on $LiNbO_3$ crystal [30], for low-loss depressed cladding waveguides, with a limited number of layers. The designs of DCWs with base layer numbers of one to six are shown in Fig. 1, where each blue ellipse indicates one laser-written track.

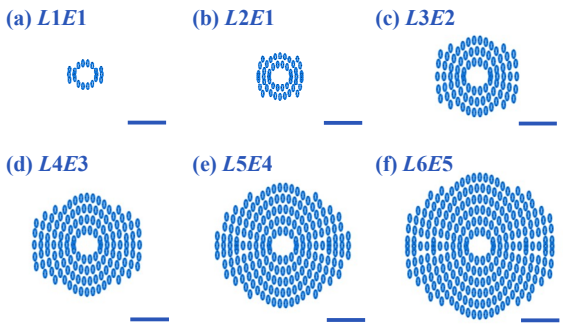

Fig. 1. (a-f) Designs of DCWs with increasing cladding-to-core ratios. In the label, the numbers after the letter *L* indicate the number of the base elliptical layers surrounding the DCW core, and the numbers after the letter *E* indicate the number of extra layers added in the horizontal direction to make the DCW cladding circular in shape. The dimensions of each track are smaller than the real dimensions for visual clarity. The blue scale bars indicate 20 µm.

Figure 2(a1-f1) shows the microscope images of six DCWs fabricated using the six designs, shown in Fig. 1(a-f). The waveguides all share the same core diameter (d_{core}) of ~10 μm [25]. The cladding diameters (d_{clad}) are summarized in Table I. As the DCWs are not perfectly symmetric, the smallest dimension of the cladding diameter was used as the d_{clad}.

B. Mode Field

Both facets of the sapphire substrate were polished to optical quality, in order to expose the fabricated waveguides. Laser light at 1550 nm from a tunable laser source (Agilent 8163A) with a single-mode fiber output (SMF28e+ equivalent) was butt-coupled into the waveguides. The near-field mode profile was recorded using an imaging system and an InGaAs camera (Hamamatsu C14041-10U). The laser polarization was

controlled with a manual polarization controller.

Light was coupled into the DCWs on a 1-cm bulk sample. Circular mode fields were observed [Fig. 2(b2-f2)]. The manual polarization controller was used to adjust the polarization of the injection light and we measured no identifiable difference between the transverse electric (TE) and transverse magnetic (TM) modes. The full-width-half-maximum (FWHM) of the mode fields are shown in Fig. 2(b2-f2). These values are larger than our previous results because of the lowered fabrication energy for crack mitigation purposes [21].

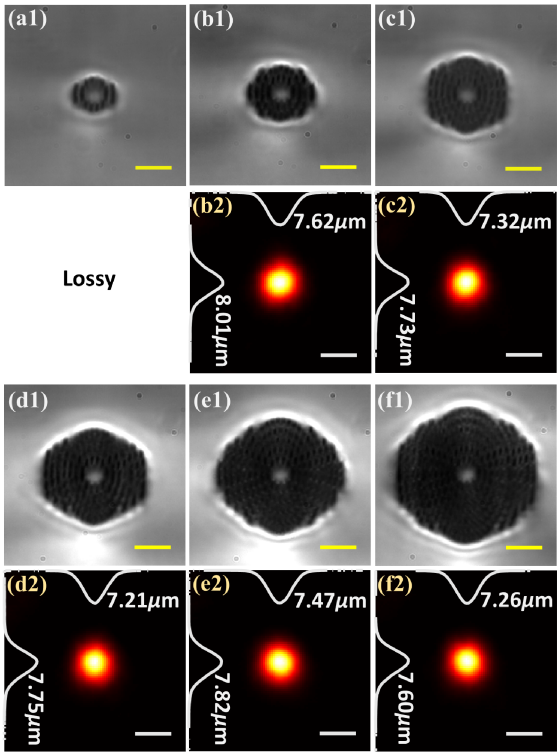

Fig. 2. Optical microscopic cross-sections (a1-f1) and measured near-field mode profiles at 1550 nm (b2-f2) of the six different single-mode sapphire DCWs, using the designs shown in Fig. 1. The DCWs have an increasing cladding-to-core diameter ratio from 3.5 (b1) to 7.9 (f1). The full-width-half-maximum dimensions of each mode profile are recorded in the labels of (b2-f2). The yellow scale bars in (a1-f1) indicate 20 μm. The white scale bars in (b2-f2) indicate 10 μm.

C. *Propagation Loss*

Propagation losses were measured using a cut-back method. A pair of DCWs were respectively fabricated on a 1-cm and a 4-cm sapphire substrate immediately after one another to keep the influence of environmental impact on the fabrication system to a minimum. The exact same fabrication parameters and design were used. The total insertion loss (TIL) consists of the coupling loss, the Fresnel loss, and the propagation loss. It was measured for both the 4-cm sample and the 1-cm samples, and then calculated to be the ratio between the measured transmitted power of the DCW and the single-mode input fiber. The coupling losses and Fresnel loss should be the same for both substrates. The propagation loss over 3 cm was calculated from the difference in the TIL by extracting these two measurements.

The transmitted power of each DCW was measured at 1550 nm. A pinhole was placed before the camera to filter out the background light. The camera was then replaced by a power meter (Newport 1919-R power meter and 818-IG detector). Three sets of DCWs with the designs of Fig. 1 were written on 1-cm and 4-cm substrates, and the averaged measurements are summarized in Table I.

Compared to the simulated propagation loss from the model described in [28], the DCWs exhibited a much larger loss experimentally. The measured loss did not decrease monotonically, despite the model predicting an exponential decrease as the cladding-to-core diameter ratio increases. Between layer numbers one and four, the propagation loss decreased as the depressed cladding diameter increased, as expected. At a cladding-to-core ratio of above five, there was an increase in propagation loss. The deviation from the theory is likely due to the more complicated refractive index distribution of the fabricated depressed cladding waveguide [30]. The femtosecond laser introduced nanograting could also induce extra scattering loss for increased cladding size [31]. Further studies will be needed to quantify the actual refractive index distribution of the waveguides, as well as the effect of scattering on the mode propagation.

TABLE I
MEASURED CLADDING AND CORE DIAMETERS, AND THE PROPAGATION LOSS OF THE DCW DESIGNS FROM FIG. 1 AND 2 (B-F).

Label in Fig. 1 and 2	Track number	d_{core} (μm)	d_{clad} (μm)	Propagation loss (dB/cm)	
				TE mode	TM mode
(b)	54	10	35	2.16	2.80
(c)	84	10	46	1.12	0.93
(d)	134	10	55	0.85	0.81
(e)	194	10	66	1.30	1.02
(f)	258	10	79	2.08	2.05

A minimum propagation loss was achieved for the four-layer plus three extra layers (*L4E3*) design shown in Fig. 1(d) and Fig. 2(d), which was measured to be 0.85 and 0.81 dB/cm for the TE and TM modes, respectively. The design consists of 134 tracks, which takes around 2 minutes to write on a 1-cm substrate. The fabrication time could be further shortened by increasing the writing speed. When coupled to a standard C-band single-mode fiber, the mode field results in a mode mismatch loss of ~0.34 dB. The cladding refractive index is calculated based on the mode profile in Fig. 1(d2). By solving the Helmholtz equation for a step index fiber, the laser-induced cladding index change is estimated to be $\Delta n_{\text{clad}} = -0.0025$. The corresponding V-number is obtained from $V = 2\pi r_{core}/\lambda\sqrt{n_{core}^2 - n_{clad}^2} = 1.89$. Since this number is lower than 2.45, single-mode operation of the waveguide is confirmed. This design was used for the WBG fabrication in the rest of the manuscript by virtue of its optimized loss.

III. FABRICATION AND CHARACTERIZATION OF THE WAVEGUIDE BRAGG GRATINGS

A. *Grating Inscription*

The WBG was created by adding an additional track with a periodic refractive index modulation in the center of the DCW core using the modulated bursts method. A 10-mm long II-order

grating was fabricated with a speed of 1 mm/s and 36-nJ pulse energy inside a 10-mm sapphire substrate. A grating period Λ of approximately the right pitch was determined by initially selecting n_{eff} to be the refractive index of bulk sapphire ($n_{sapphire}$ = 1.7462 at 1550 nm). The grating period was 887.64 nm long. The position synchronized output (PSO) control function of the Aerotech stage was used to further window the 1 MHz laser output into a burst train with a repetition rate f_{rep} [32], calculated by

$$f_{rep} = \frac{v}{\Lambda} \quad (2)$$

where v was the stage translation speed. A duty cycle of 1% was used, which was equivalent to 8 overlapping pulses per grating element.

Figure 3(a) shows the top view of the waveguide and Bragg grating. The periodic index modulated track can be visibly identified in the magnified top view of the core region [Fig. 3(b)]. The cross-section is shown in Fig. 3(c), with the extra track in the DCW center as compared to Fig. 2(d1). The fabrication was programmed to make sure all the tracks were written from bottom to top. The Bragg grating was fabricated in 10 seconds on a 1-cm chip. The speed can be further increased by using a faster writing speed.

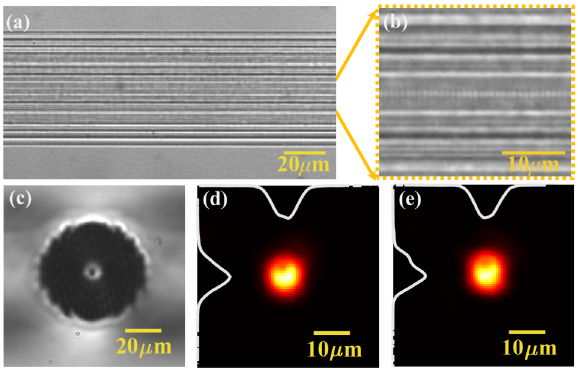

Fig. 3. (a) The top view of a II-order WBG inscribed inside a DCW. The DCW has a 55-μm diameter cladding and 10-μm diameter core, and the WBG has a period of 887.64 nm, (b) a magnified top view of the waveguide core area in (a), showing the grating pitch, (c) the cross-sectional view of the WBG, with the grating track in the center of the DCW, (d-e) the near-field mode profiles for the TE (d) and TM (e) polarizations.

B. Spectral Performance Characterization

The end facets of the sapphire substrate were polished to optical quality to expose the start and end of the WBGs. An Agilent 8164A swept tunable laser source and photodetector system were connected to the WBG using a single-mode optical circulator for spectral measurements. Index matching oil (n = 1.518) was applied between the launch fiber (Corning SMF28e+ equivalent) and the sapphire substrate, in order to reduce the Fresnel reflection and Fabry-Pérot cavity effect created by the polished substrate facets. Figure 3(d) and Fig. 3(e) show the mode fields for the TE and TM modes, respectively. Compared to the waveguides in Fig. 2(d), the mode field of the WBG was distorted slightly by the refractive index modulation track at the core center.

The reflection spectra are shown in Fig. 4. They were recorded by sweeping the input laser wavelength from 1545 to 1552 nm with a 10 pm step size for both polarizations. Distinct reflection peaks are identifiable for each of the two polarization modes. Here the Bragg wavelengths were measured to be 1547.95 nm and 1549.17 nm for the TE and TM modes, respectively. These numbers correspond, respectively, to an effective refractive index of 1.7439 and 1.7453, based upon a grating period of 887.64 nm. The reflectivity power is also plotted in a decibel scale in Fig. 5(a). The signal to noise ratio (SNR) of the reflected power above the noise floor was measured to be higher than 15 dB for both the TE and TM polarizations, which could be further improved with better mode matching and anti-reflection coating to reduce the noise floor. The transmission spectra were measured using the same method as that described in Part II to measure the transmission loss. Figure 5(b) shows transmission spectra for both polarizations, plotted in a decibel scale. The 3-dB bandwidths were measured to be 0.137 and 0.132 nm for the TE and TM polarizations, respectively. The bandwidth between the first minima of the Bragg reflection response can be determined analytically from the coupled-mode equations [33]. This yields values of 0.153 and 0.157 nm for the two polarizations. However, the experimental zero-to-zero bandwidth appears to be slightly wider than ~ 0.55 and 0.62 nm. One reason for this may be due to variability in the stage translation speed over the length of the grating.

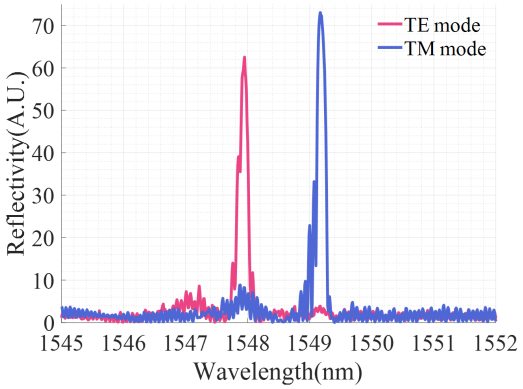

Fig. 4. The reflection spectra of a 10-mm long, II-order WBG in Fig. 3, for both polarizations. The fabrication parameters were set to 36 nJ pulse energy, 1 mm/s writing speed, and a 1% duty cycle. The spectra were measured using a tunable laser source and photodetector system and a circulator. The Bragg wavelengths for the TE (pink) and TM polarizations (blue) are 1547.95 and 1549.17 nm, respectively.

C. Grating Loss

Waveguide Bragg gratings with different lengths ranging from 1 mm to 40 mm were written inside DCWs with the same design inside both 10-mm and 40-mm sapphire substrates. These WBGs were fabricated within the same hour to reduce the influence of environmental impact. The transmitted powers were measured at the out-of-band wavelength of 1550 nm using the same method as described in Part II. The grating loss (dB/cm) was inferred from the following equation: $\alpha_{TIL} = \alpha_{coupling} + \alpha_{DCW}(L - l_{WBG}) + \alpha_{WBG} l_{WBG}$ where α_{TIL} and $\alpha_{coupling}$ are the total insertion loss and the coupling loss, respectively, in the unit of dB, α_{DCW} and α_{WBG} are the propagation loss of the DCW and the WBG, respectively, in

units of dB/cm, L is the total length of the substrate, and l_{WBG} is the length of the grating. The values of α_{DCW} measured in Part II were used. Assuming consistent Fresnel and coupling losses for each WBG and by using a linear fit, the loss was estimated to be 1.50 dB/cm for the TE mode and 1.40 dB/cm for the TM mode.

D. Coupling Coefficient

The reflectivity was calculated from the transmission spectra of both TE and TM polarizations in Fig. 5(b). The power reflectivity at the Bragg wavelength was calculated using [34]

$$R_{\lambda_B} = 1 - 10^{-\frac{T}{10}} = \tanh^2(\kappa L) \quad (3)$$

where T is the depth of the transmission dips at the Bragg wavelengths, which were measured to be 7.78 and 9.15 dB between the transmission power at the Bragg resonance and at 1550 nm. Using Eq. (3), the peak reflectivity was calculated to be 83.3% and 87.8% for TE and TM modes, respectively. The coupling coefficients were found, respectively, to be 154.45 and 171.49 m^{-1}, yielding a grating strength, κL equal to 1.54 and 1.72, respectively. These strengths are comparable to WBGs written in crystals such as Yb-doped YAG [35], lithium niobate [36], and diamond [37].

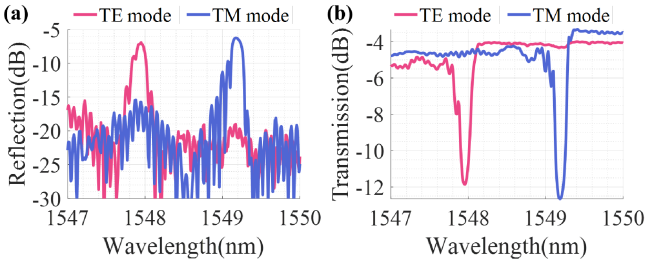

Fig. 5. (a) The reflection spectra of the WBG from Fig. 4 plotted in a decibel scale over a 3 nm wavelength range, for both TE (pink) and TM (blue) polarizations, and (b) the transmission spectra of the same WBG, showing a transmission dip of 7.78 and 9.15 dB for the TE and TM polarizations, respectively.

E. Birefringence

The birefringence of the WBG is calculated to be -1.4×10^{-3} from $\Delta n_b = (\lambda_{B\,TE} - \lambda_{B\,TM})/2\Lambda$ [6], where Δn_b is the birefringence, $\lambda_{B\,TE}$ and $\lambda_{B\,TM}$ are the Bragg wavelengths for the two orthogonal polarizations. It is unlikely that the birefringence is caused by the sapphire intrinsic birefringence or the DCW, as the DCW direction is along the sapphire optical axis, and we observed almost identical mode profiles for both the TE and TM polarizations (c.f., Fig. 3). We attribute this Bragg wavelength splitting to the influence from the center WBG track and propose three possible origins, which are described as follows.

Firstly, the addition of the modulated refractive index track in the core center will introduce an additional anisotropic stress field, causing a polarization-dependent refractive index distribution from the stress-optic effect [38]. Secondly, due to the elliptical shape of the laser focal volume, the refractive index distribution and indices are different along the horizontal and vertical directions across the grating track. And thirdly, the formation of self-aligned nanogratings at the laser focus can also introduce form birefringence at a similar scale [31], [39]. While birefringence could be desirable for creating polarization-sensitive devices, it is also undesirable for applications such as high accuracy temperature sensing. We demonstrate in Part IV that the birefringence can be mitigated by thermal annealing.

IV. Annealing

A II-order WBG was inscribed using a pulse energy of 28 nJ with 1% duty cycle, from end to end on a 1-cm long sapphire substrate. Before the measurement, the sapphire substrate was kept at room temperature for three months. No obvious changes in the spectra were observed when re-measuring. The WBG was then heated inside a box furnace. This involved increasing the temperature to 1000°C over a duration of six hours, holding it at 1000°C for one hour, before cooling it down to room temperature at the natural cooling rate.

Figure 6 shows the reflection spectra for the TE and TM modes after fabrication (plotted in blue) and after the 1000°C annealing (plotted in yellow). The residual stress was relieved for both polarizations after the first annealing, causing the Bragg wavelength to red shift in both cases. A wavelength red shift of 1.20 nm from 1547.97 to 1549.17 nm was observed in the TE mode spectra whereas the TM mode experienced a red shift that was much smaller at only 0.04 nm.

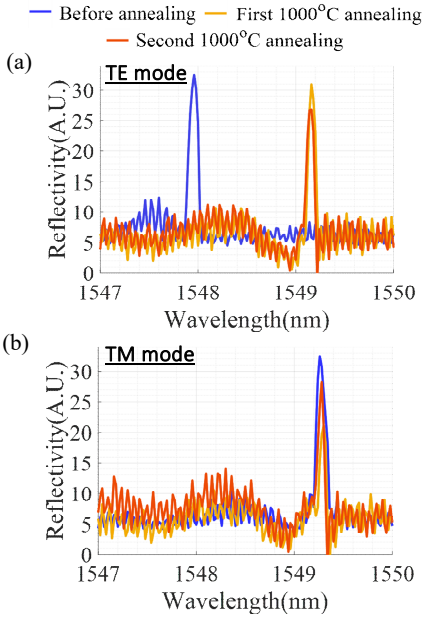

Fig. 6. Thermal properties of the reflection spectra for the (a) TE and (b) TM modes of a WBG before annealing (blue), after the first round of annealing at 1000°C (yellow), and after a second round of annealing at 1000°C (orange). The birefringence decreased from 1.47×10^{-3} to 0.16×10^{-3} after the first round of annealing, and remained unchanged after the second round of annealing.

The wavelength shift can be attributed to two mechanisms. Annealing causes the release of the anisotropic stress field introduced during the fabrication [38], as well as the weakening of the laser-introduced refractive index change [24]. Overall, the birefringence decreased from 1.47×10^{-3} to 0.16×10^{-3} after the first annealing process.

A second annealing step was conducted to test whether the wavelength shift was permanent. The annealed sample was placed back inside the furnace to be annealed at 1000°C following the same temperature rise and drop cycle as before. After this second round of annealing, effective guiding was still visible, and no identifiable wavelength shift or peak reflectivity change was measured as compared to the first round of annealing, as shown in the orange plots in Fig. 6. Moreover, the birefringence remained the same, indicating that the stress release is a one-time shift. Fabry-Pérot fringes could be seen in all the spectra as we did not apply index matching fluid. Fourier analysis of the spectra showed the fringes were due to a 10-mm long cavity within the sapphire, caused by reflection between the substrate facets.

Table II summarizes the Bragg wavelength and the effective refractive index, calculated using Eq. (1), during the thermal tests. A Burneman frequency estimation method was used to more accurately calculate the Bragg wavelengths [40]. There remains a very small birefringence of 0.16×10^{-3} after annealing and stress release.

TABLE II
SUMMARY OF WBG PROPERTIES BEFORE ANNEALING, AFTER THE FIRST ANNEALING STEP, AND AFTER THE SECOND AND THIRD ANNEALING STEPS.

	TE mode		TM mode		Birefringence Δn_b
	λ_B (nm)	n_{eff}	λ_B (nm)	n_{eff}	
Before annealing	1547.970	1.7437	1549.271	1.7452	1.47×10^{-3}
After 1st annealing	1549.171	1.7450	1549.310	1.7452	0.16×10^{-3}
After 2nd annealing	1549.170	1.7450	1549.309	1.7452	0.16×10^{-3}
Annealing at 1200°C	1549.352	1.7455	1549.441	1.7456	0.10×10^{-3}

With the high melting point of sapphire of over 2000°C, it is desirable to verify the performance of the grating under even higher temperature. The previously annealed sample was kept at room temperature for 18 months before the test. The spectra were measured for both polarizations. No identifiable changes in the Bragg wavelength and peak intensity were observed. The grating was put inside the furnace and raised up to 1200°C at a ramp rate of 10°C/min. It was annealed in the furnace under 1200°C for 3 hours, before being cooled down to room temperature. The reflection spectra were measured. The results are summarized in Table II. There was no identifiable change in the peak reflectivity magnitude. The polarization splitting was 89 pm. The birefringence was further reduced to 1.0×10^{-4}.

Following our analysis in Part III, this is due to either the asymmetric refractive index distribution or the form birefringence introduced by the grating track in the DCW core center. Possible solutions for reducing this birefringence include creating a more symmetric and uniform mode overlapping area by using plane-by-plane laser scanning [41] or by beam shaping [42], and by using circular polarized light during fabrication [40]. So far, we have shown that once annealed, the WBG robustly survived a temperature of 1200°C with a permanent decrease in the grating birefringence. Further investigations are still needed to understand the underlying mechanisms and to test the thermal properties under a higher temperature.

V. GRATING OPTIMIZATION CONSIDERATIONS

In this part, we demonstrate quantitatively the optimization of WBG reflectivity based on grating design and fabrication parameters. A laser pulse energy of 28 nJ, a repetition rate of 1 MHz, and a writing speed of 11 mm/s, were used to fabricate the DCWs which enclosed the gratings, using the design shown in Fig. 1(d) and Fig. 2(d). The WBGs were written on a 10-mm sapphire substrate.

The polarization of the input light was controlled using a manual polarization controller. A very similar dependence was observed in terms of reflectivity and grating bandwidth on the optimization parameters for both TE and TM modes, and thus we omitted the results from the TE modes for clarity. Only the spectra of the TM modes are presented in the following subsections.

A. Grating Length

Second-order gratings with a length between 1 to 10 mm were written using a pulse energy of 30 nJ, a translation speed of 1 mm/s and a duty cycle of 1%. Figure 7(a) shows the reflection spectra for the TM modes measured at a step resolution of 10 pm. The peak reflectivity increases as the WBG length increases from 1 to 6 mm. It saturates at a length of 6 mm, then starts to decrease slightly as the length further increases.

The transmission spectra are shown in Fig. 7(b). Offsets were added to each spectrum for clarity. From Eq. (3), the grating reflectivity increases monotonically with the increase of the grating length, from 41.9% for a 4 mm WBG to 77.5% for a 10 mm WBG. The deviation between the peak reflectivity measured from the reflection and transmission spectra is likely a result of the double-pass propagation loss.

The reflectivity of each WBG is calculated from its transmission spectrum and is plotted in the inset of Fig. 7(b) using blue squares. An estimation of the peak reflectivity's dependence on the grating length was plotted in the dashed line, by using the coupling coefficient of 171.49 m^{-1}, as found in Part III. We expect the grating reflectivity to continue to increase as we further increase the grating length to be over 10 mm.

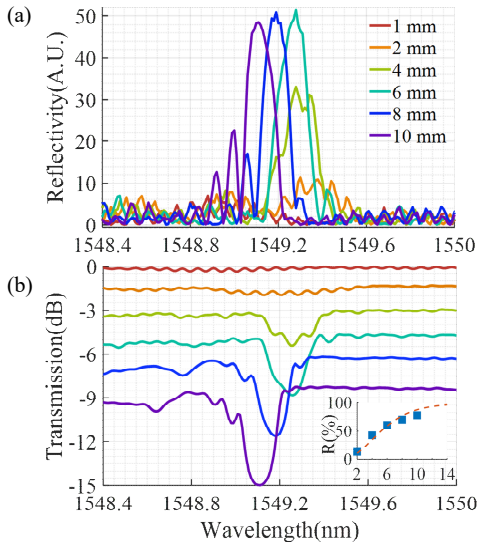

Fig. 7. (a) Reflection and (b) transmission spectra of II-order WBGs, fabricated 4using 28 nJ pulse energy, and a 1% duty cycle with different grating lengths from 1 to 10 mm. Offsets were added to each spectrum in (b) for better visual clarity. The inset of (b) shows the reflectivity calculated from (blue squares) and the simulated the peak reflectivity (orange dashed lines) vs. the length of the grating in units of mm. The spectra are for TM polarization only.

B. Pulse Energy

Second-order WBGs with a length of 10 mm were written using a 1 mm/s writing speed and five different pulse energies ranging between 20 and 83 nJ. The corresponding reflection and transmission spectra are shown in Fig. 8. The threshold pulse energy is found to be 15 nJ, which is the minimum pulse energy required to create an observable refractive index modification inside the sapphire substrate. Between 15 nJ and around 36 nJ, increasing the pulse energy leads to a rapid growth in the peak reflectivity. However, as the pulse energy further increases above 46 nJ, the peak reflectivity decreases.

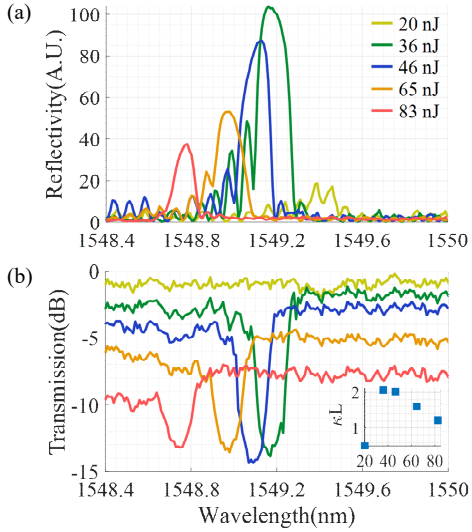

Fig. 8. Reflection (a) and transmission (b) spectra of II-order, 10-mm long WBGs fabricated with increasing pulse energies ranging from 20 to 83 nJ, for TM polarization only. Inset of (b) shows the product of the coupling coefficient and the grating length (10 mm) vs. the fabrication pulse energy. The unit of the *x* axis is nJ.

An insight into these observations can be found in Fig. 9. Different orders of gratings were inscribed at varying pulse energies without the surrounding DCW. The gratings were written using a duty cycle of 1% and a writing speed of 1 mm/s. The case for the II-order gratings can be seen from the middle row in Fig. 9. From right to left, the tracks became darker as the effective refractive index n_{eff} becomes more negative, causing the Bragg wavelength to blue shift with the increase of the pulse energy, which is consistent with the trend shown in Fig. 8.

As seen from Eq. (3), the peak reflectivity is dependent on the product of the coupling coefficient κ and the grating length L. The coupling coefficient κ is given by [1]

$$\kappa = \frac{\pi}{\lambda_B}\Delta n g(z)\eta \tag{4}$$

where Δn is the refractive index modulation, $g(z)$is the apodization function, and η is the mode overlap factor. The refractive index changes can be assessed from the contrast between laser-introduced modifications and the substrate in Fig. 9 [43].

Changing the laser pulse energy increases both the amplitude and the dimension of the refractive index change of each period element. Above the threshold energy, as the pulse energy increases, the modulation amplitude becomes stronger with increasing refractive index change. However, as the pulse energy passes the optimum value, the adjacent periods start to overlap with each other, the index modulation amplitude saturates and decreases, as can be seen from the tracks written using the higher pulse energies in the left columns of Fig. 9. From Fig. 8, the optimum pulse energy giving the highest peak reflectivity for a II-order grating lies in the region between 20 to 46 nJ.

Differences between the transmission power at 1550 nm and the Bragg resonance wavelength are measured to be 12.02, 11.63, and 8.3 dB for the WBGs fabricated using a pulse energy of 36, 46, and 65 nJ, respectively. From Eq. (3), the reflectivity is calculated to be 93.7%, 93.1%, and 85.0%, with corresponding coupling coefficients of 206.12, 201.40, and 160.27 m^{-1}.

The products of the coupling coefficient and the grating length are plotted in the inset of Fig. 8(b), with the highest κL being 2.06. By further increasing the grating length, a strong grating with $\kappa L > 3$ may be possible. The 3-dB bandwidths for the WBGs written with 36, 46, and 65 nJ are measured to be 0.110, 0.111, and 0.123 nm, respectively.

While the grating written using a pulse energy of 36 nJ has a similar level of transmission dip amplitude to the grating written using a pulse energy of 46 nJ, the peak reflectivity of the former appears to be slightly higher, as a result of the increased grating loss with the increased fabrication pulse energy. This effect can also be observed from the decreased background transmission level with the increase of laser pulse energy in Fig. 8(b). Further optimization in terms of the coupling coefficient and the loss is possible following similar processes developed for the silica platforms [44].

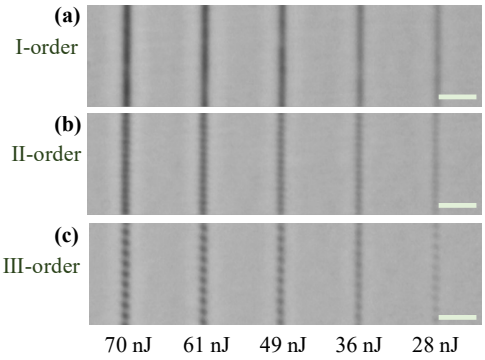

Fig. 9. Top views of grating tracks without the surrounding DCWs for (a) I, (b) II, and (c) III orders, fabricated using pulse energies of 28, 36, 49, 61, and 70 nJ from left to right, and a duty cycle of 1%. The scale bars are 5 μm.

C. Grating Order

While increasing the grating length can increase the peak reflectivity, a longer grating may not be desirable for applications such as sensing. An alternative method is to increase the coupling coefficient, which can be achieved by creating a grating with a lower order number. Waveguide Bragg grating which are 10-mm long and of orders of I, II, and IV were written using 28 nJ pulse energy and 1 mm/s writing speed. A duty cycle of 1% was used for all the grating orders, which corresponded to 4, 8, and 16 pulses per pitch, respectively. Figure 10 shows the reflection and transmission spectra of the gratings for the TM polarization.

Theoretically, the peak reflectivity should decrease as the grating order is increased, since the relative magnitude of the Fourier coefficients of the pitch decrease with each harmonic. However, the peak reflectivity achieves its maximum value for the II-order, then decreases only slightly for the IV-order grating. As shown in Fig. 9, the higher coupling coefficients of the lower-order gratings were balanced by a decrease in the refractive index modulation amplitude Δn due to the overlap between adjacent pitches with a smaller spacing. An optimum combination of the laser pulse energy, duty cycle, laser focus dimension, and grating length needs to be considered for each grating order number.

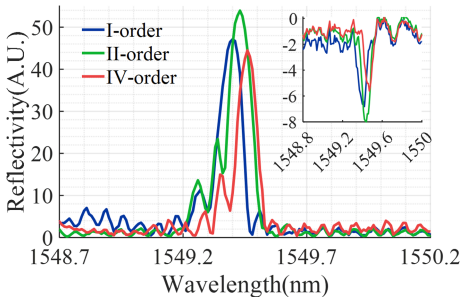

Fig. 10. The reflection spectra of 10-mm long, I, II, and IV-order WBGs fabricated using 28 nJ pulse energy, and a 1% duty cycle. The inset shows the transmission spectra of the same WBGs. The *y*-axis is the transmission in units of dB. The *x*-axis is the wavelength in units of nm. The spectra are for TM polarization only.

We have also investigated the influence of other optimization factors such as the number of pulses per pitch, duty cycle, translation speed and repetition rate. However, it was found that an optimum combination of grating length, order, and pulse energy could effectively enable the flexibility of tailoring the WBG's spectral performance. A tailoring of the bandwidth is achievable but not demonstrated here, as the spectra become deteriorated by the Fabry-Pérot fringes caused by the reflection between sapphire end-facets. This could potentially be resolved by angle polishing both sapphire facets or through the use of anti-reflection coatings. We expect further improvement in the peak reflectivity and more precise tailoring of the bandwidth to be achievable by finer tuning of design and fabrication parameters.

VI. Potential for More Complex Grating Designs

A useful type of grating is the sampled grating. These gratings contain periodic gaps in the refractive index modulation. The resulting spectra contain wavelengths with equal spacing $\Delta\lambda_S$ about the Bragg resonance wavelength according to

$$\Delta\lambda_S = \frac{\lambda_B^2}{2n_{eff}\Lambda_S} \tag{5}$$

where Λ_S is the sampling period of the gaps. Sampled gratings have been used in distributed Bragg reflector lasers for wide wavelength tuning and they have a broad range of applications in optical communications and sensing [45].

An amplitude modulated sampled grating was fabricated on a 1-cm sapphire substrate by writing a 1-cm long I-order WBG. The WBG was fabricated within a DCW with the design described in Part III and the optimized fabrication parameters. The design Bragg wavelength was 1550 nm, with a duty cycle of 50% and a modulation period of 200 μm. In this representative case, the wavelength spacing $\Delta\lambda_S$ was calculated to be 3.43 nm from Eq. (5). Figure 11 shows the spectrum measured between 1520 and 1580 nm at a resolution of 20 pm, showing that the WBG written using the modulated bursts inside single-mode DCW can support complex grating designs in crystalline materials.

Another advantage of our WBG fabrication technique is that it allows narrow bandwidths to be realized. This provides the potential for precise wavelength determination for more accurate sensing and dense multiplexing. An array of 7 WBGs were fabricated on a 4-cm sapphire chip in a single scan, using a pulse energy of 28 nJ, a writing speed of 1 mm/s, and a 1% duty cycle. The designed Bragg resonance wavelengths for the gratings, in the order of their positions along the sapphire substrate, were 1549, 1552, 1555, 1558, 1561, 1564, and 1567 nm, respectively. All the WBGs were I-order and 3 mm in length. The center-to-center spacing was 3 mm. The WBGs were written within a DCW which used the same design and fabrication parameters as described in Part III.

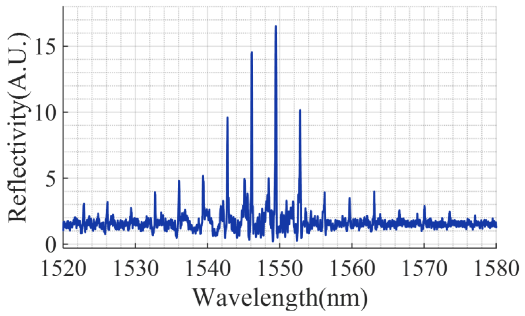

Fig. 11. Reflection spectrum (TM polarization) of a I-order, 10-mm long amplitude-modulated sampled-grating with a modulation period of 200 μm.

Figure 12 shows the spectrum of the WBGs for the TM polarization. As the spectrum was measured from the side closer to the gratings with the shorter Bragg wavelengths, a decrease in the peak reflectivity with the increased Bragg wavelength was observed. The Bragg peaks are evidently impacted by fringes, which could be mitigated using the approaches described above. The overlapped orange line shows the spectrum filtered with a simple low-pass digital filter to remove the Fabry-Pérot cavity fringes. However, despite the fringes, the reflection peaks are clearly identifiable.

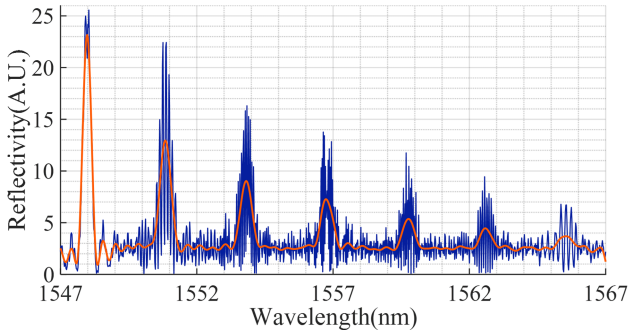

Fig. 12. Reflection spectrum of 7 multiplexed WBGs (dark blue) spanning a 20 nm spectral range (TM polarization). The WBGs were written on a 4-cm long sapphire substrate. Each grating is I-order and 3 mm long. A low-pass filter was used to filter the fringes in the spectrum. The filtered spectrum (orange) overlaps on top of the original spectrum.

VII. Conclusions

We have demonstrated the fabrication and optimization of waveguides and Bragg gratings on single-crystal sapphire substrates. Single-mode waveguides were fabricated using femtosecond laser direct writing with adaptive optics. While DCWs have been known for their high radiative loss due to the limited cladding size, we demonstrated the possibility to decrease the DCW propagation loss to as low as 0.8 dB/cm by increasing the cladding diameter, using an optimized geometry design.

Within the optimized single-mode waveguides, Bragg gratings designed for operation at the telecommunications C-band were written using the modulated bursts method. The following advantages were demonstrated as compared to our previous ring-by-ring method [25]: 1) the design is simpler, and thus more robust to the environmental changes during fabrication; 2) the fabrication speed is higher (more than 700 times faster), which enables the inscription of more complex grating structures at better efficiency; and 3) the method allows the flexibility in tailoring the WBG spectral responses, in terms of reflectivity and bandwidth.

We reported the optimization of the WBGs on a 1-cm sapphire platform by tuning the grating design and laser fabrication parameters. A high reflectivity of up to 93%, a κL higher than 2, and ultralow 3-dB bandwidths of below 0.15 nm were achieved. Further optimization of the bandwidth will also be possible with improved anti-reflection methods.

Thermal stability was demonstrated through repeated annealing tests at 1000°C. Annealing also had the effect of lowering the birefringence to 1.6×10^{-4}. These results can provide experimental guidance on fabricating low-birefringent and high-reflectivity WBGs. Finally, combining the advantages of the optimized single-mode waveguide and grating, a sampled-grating and an array of seven gratings were demonstrated to showcase the possibilities enabled by our method.

The techniques described herein show great potential for fabricating low-loss single-mode Bragg gratings and waveguides with narrow bandwidth and high reflectivity in sapphire substrates. These techniques also have application to other crystalline substrates, enabling many potential applications such as laser delivery, telecommunications, and sensing.

Acknowledgment

The authors gratefully acknowledge the support and advice of their partners Rolls-Royce plc., Cranfield University, UK Atomic Energy Authority and MDA Space and Robotics. The authors thank Miss Diana Passmore for the use of the furnace. They thank Professor Dominic O'Brien, Dr Andy Schreier, and Dr Fabian Pokorny for the use of optical equipment.

References

[1] M. Ams, P. Dekker, S. Gross, and M. J. Withford, "Fabricating waveguide Bragg gratings (WBGs) in bulk materials using ultrashort laser pulses," *Nanophotonics*, vol. 6, no. 5, pp. 743–763, Aug. 2017, doi: 10.1515/NANOPH-2016-0119.

[2] C. D. Lines *et al.*, "Fiber Bragg-Grating True Time-Delay Systems : Discrete-Grating Array 3-b Delay Lines," vol. 45, no. 8, pp. 1527–1530, 1997.

[3] M. Zaghloul *et al.*, "Radiation resilient fiber Bragg grating sensors for sensing applications in nuclear reactor cores," in *Proceedings of SPIE - The International Society for Optical Engineering*, 2018. doi: 10.1117/12.2296458.

[4] M. J. Withford, M. Ams, P. Dekker, J. A. Piper, and G. D. Marshall, "Directly written monolithic waveguide laser incorporating a distributed feedback waveguide-Bragg grating," *Optics Letters, Vol. 33, Issue 9, pp. 956-958*, vol. 33, no. 9, pp. 956–958, May 2008, doi: 10.1364/OL.33.000956.

[5] A. Martinez, M. Dubov, I. Khrushchev, and I. Bennion, "Direct writing of fibre Bragg gratings by femtosecond laser," *Electronics Letters,* vol. 40, no. 19, p. 1, Sep. 2004, doi: 10.1049/el:20046050.

[6] G. D. Marshall, M. Ams, and M. J. Withford, "Direct laser written waveguide-Bragg gratings in bulk fused silica," *Opt Lett*, vol. 31, no. 18, p. 2690, Sep. 2006, doi: 10.1364/OL.31.002690.

[7] H. Zhang, S. M. Eaton, and P. R. Herman, "Single-step writing of Bragg grating waveguides in fused silica with an externally modulated femtosecond fiber laser," *Opt Lett*, vol. 32, no. 17, p. 2559, Sep. 2007, doi: 10.1364/OL.32.002559.

[8] G. Roth, S. Hessler, S. Kefer, … M. G.-O., and undefined 2020, "Femtosecond laser inscription of waveguides and Bragg gratings in

transparent cyclic olefin copolymers," *opg.optica.org*, Accessed: Feb. 26, 2023. [Online]. Available: https://opg.optica.org/abstract.cfm?uri=oe-28-12-18077

[9] C. Denz, J. Imbrock, L. Wesemann, M. Ayoub, and S. Kroesen, "Waveguide-integrated three-dimensional quasi-phase-matching structures," *Optica, Vol. 7, Issue 1, pp. 28-34*, vol. 7, no. 1, pp. 28–34, Jan. 2020, doi: 10.1364/OPTICA.7.000028.

[10] G. M. Katyba *et al.*, "Sapphire shaped crystals for waveguiding, sensing and exposure applications," *Progress in Crystal Growth and Characterization of Materials*, vol. 64, no. 4, pp. 133–151, Dec. 2018, doi: 10.1016/J.PCRYSGROW.2018.10.002.

[11] H. Chen, M. Buric, P. R. Ohodnicki, J. Nakano, B. Liu, and B. T. Chorpening, "Review and perspective: Sapphire optical fiber cladding development for harsh environment sensing," *Appl Phys Rev*, vol. 5, no. 1, Mar. 2018, doi: 10.1063/1.5010184.

[12] S. J. Mihailov, "Fiber bragg grating sensors for harsh environments," *Sensors*, vol. 12, no. 2, pp. 1898–1918, Feb. 2012, doi: 10.3390/S120201898.

[13] H. Aakre, T. Solbakken, and R. B. Schüller, "An in-line NIR/endoscope technique for observations in real hydrocarbon multiphase systems," *Flow Measurement and Instrumentation*, vol. 16, no. 5, pp. 289–293, Oct. 2005, doi: 10.1016/J.FLOWMEASINST.2005.03.004.

[14] Z. Cheng *et al.*, "Mid-infrared grating couplers for silicon-on-sapphire waveguides," *IEEE Photonics J*, vol. 4, no. 1, pp. 104–113, 2012, doi: 10.1109/JPHOT.2011.2179921.

[15] G. Lin and Y. Huang, "High Mechanical Strength Sapphire Cover Lens for Smartphone Screen," *Crystal Research and Technology*, vol. 53, no. 7, pp. 1–5, 2018, doi: 10.1002/crat.201800049.

[16] D. Grobnic, S. J. Mihailov, C. W. Smelser, and H. Ding, "Sapphire fiber bragg grating sensor made using femtosecond laser radiation for ultrahigh temperature applications," *IEEE Photonics Technology Letters*, vol. 16, no. 11, pp. 2505–2507, Nov. 2004, doi: 10.1109/LPT.2004.834920.

[17] A. Graf, H. Bartelt, M. Rothhardt, T. Elsmann, and T. Habisreuther, "Inscription of first-order sapphire Bragg gratings using 400 nm femtosecond laser radiation," *Optics Express, Vol. 21, Issue 4, pp. 4591-4597*, vol. 21, no. 4, pp. 4591–4597, Feb. 2013, doi: 10.1364/OE.21.004591.

[18] S. Yang, D. Hu, and A. Wang, "Point-by-point fabrication and characterization of sapphire fiber Bragg gratings," *Opt Lett*, vol. 42, no. 20, p. 4219, Oct. 2017, doi: 10.1364/OL.42.004219.

[19] X. Xu *et al.*, "Sapphire fiber Bragg gratings inscribed with a femtosecond laser line-by-line scanning technique," *Opt Lett*, vol. 43, no. 19, p. 4562, Oct. 2018, doi: 10.1364/OL.43.004562.

[20] V. Apostolopoulos *et al.*, "Femtosecond-irradiation-induced refractive-index changes and channel waveguiding in bulk Ti3+: Sapphire," *Appl Phys Lett*, vol. 85, no. 7, pp. 1122–1124, 2004, doi: 10.1063/1.1781737.

[21] C. Grivas *et al.*, "Generation of Multi-Gigahertz Trains of Phase-Coherent Femtosecond Laser Pulses in Ti:Sapphire Waveguides," *Laser Photon Rev*, vol. 12, no. 11, p. 1800167, Nov. 2018, doi: 10.1002/LPOR.201800167.

[22] Y. Ren, L. Zhang, H. Xing, C. Romero, J. R. Vázquez de Aldana, and F. Chen, "Cladding waveguide splitters fabricated by femtosecond laser inscription in Ti:Sapphire crystal," *Opt Laser Technol*, vol. 103, pp. 82–88, Jul. 2018, doi: 10.1016/J.OPTLASTEC.2018.01.021.

[23] Y. Ren *et al.*, "Optical-lattice-like waveguide structures in Ti:Sapphire by femtosecond laser inscription for beam splitting," *Opt Mater Express*, vol. 7, no. 6, p. 1942, 2017, doi: 10.1364/ome.7.001942.

[24] J.-P. Bérubé, J. Lapointe, A. Dupont, M. Bernier, and R. Vallée, "Femtosecond laser inscription of depressed cladding single-mode mid-infrared waveguides in sapphire," *Opt Lett*, vol. 44, no. 1, p. 37, 2019, doi: 10.1364/ol.44.000037.

[25] P. S. Salter *et al.*, "Single-mode sapphire fiber Bragg grating," *Optics Express, Vol. 30, Issue 9, pp. 15482-15494*, vol. 30, no. 9, pp. 15482–15494, Apr. 2022, doi: 10.1364/OE.446664.

[26] S. Kefer, G. L. Roth, J. Zettl, B. Schmauss, and R. Hellmann, "Sapphire Photonic Crystal Waveguides with Integrated Bragg Grating Structure," *Photonics*, vol. 9, no. 4, 2022, doi: 10.3390/photonics9040234.

[27] L. Huang, P. Salter, M. Karpiński, B. Smith, F. Payne, and M. Booth, "Waveguide fabrication in KDP crystals with femtosecond laser pulses," *Appl Phys A Mater Sci Process*, vol. 118, no. 3, pp. 831–836, 2015, doi: 10.1007/s00339-014-8899-9.

[28] L. G. Cohen, D. Marcuse, and W. L. Mammel, "Radiating Leaky-Mode Losses in Single-Mode Lightguides with Depressed-Index Claddings," *IEEE Trans Microw Theory Tech*, vol. 30, no. 10, pp. 1455–1460, 1982, doi: 10.1109/TMTT.1982.1131277.

[29] V. Mezentsev, I. Bennion, A. Shestakov, and A. Okhrimchuk, "Low loss depressed cladding waveguide inscribed in YAG:Nd single crystal by femtosecond laser pulses," *Optics Express, Vol. 20, Issue 4, pp. 3832-3843*, vol. 20, no. 4, pp. 3832–3843, Feb. 2012, doi: 10.1364/OE.20.003832.

[30] H.-D. Nguyen *et al.*, "Low-loss 3D-laser-written mid-infrared LiNbO_3 depressed-index cladding waveguides for both TE and TM polarizations," *Opt Express*, vol. 25, no. 4, p. 3722, 2017, doi: 10.1364/oe.25.003722.

[31] S. Xu *et al.*, "Ultrafast laser-inscribed nanogratings in sapphire for geometric phase elements," *Opt Lett*, vol. 46, no. 3, p. 536, Feb. 2021, doi: 10.1364/OL.413177.

[32] "Position Synchronized Output (PSO) | Aerotech." Accessed: Dec. 12, 2023. [Online]. Available: https://www.aerotech.com/position-synchronized-output-pso-coordinate-part-position-with-process-control/

[33] I. Bennion, J. A. R. Williams, L. Zhang, K. Sugden, and N. J. Doran, "Uv-written in-fibre Bragg gratings," *Opt Quantum Electron*, vol. 28, no. 2, Feb. 1996, doi: 10.1007/BF00278281.

[34] T. Erdogan, "Fiber grating spectra," *Journal of Lightwave Technology*, vol. 15, no. 8, pp. 1277–1294, Aug. 1997, doi: 10.1109/50.618322.

[35] M. J. Withford, M. Ams, T. Calmano, P. Dekker, and C. Kränkel, "2 W single-longitudinal-mode Yb:YAG distributed-feedback waveguide laser," *Optics Letters, Vol. 42, Issue 14, pp. 2734-2737*, vol. 42, no. 14, pp. 2734–2737, Jul. 2017, doi: 10.1364/OL.42.002734.

[36] S. Kroesen, W. Horn, J. Imbrock, and C. Denz, "Electro–optical tunable waveguide embedded multiscan Bragg gratings in lithium niobate by direct femtosecond laser writing," *Opt Express*, vol. 22, no. 19, p. 23339, 2014, doi: 10.1364/oe.22.023339.

[37] V. Bharadwaj *et al.*, "Femtosecond laser inscription of Bragg grating waveguides in bulk diamond," *ArXiv*, vol. 42, no. 17, pp. 3451–3453, 2017, doi: 10.1364/ol.42.003451.

[38] H.-D. Nguyen *et al.*, "Heuristic modelling of laser written mid-infrared LiNbO_3 stressed-cladding waveguides," *Opt Express*, vol. 24, no. 7, p. 7777, 2016, doi: 10.1364/oe.24.007777.

[39] C. He *et al.*, "Revealing complex optical phenomena through vectorial metrics," *https://doi.org/10.1117/1.AP.4.2.026001*, vol. 4, no. 2, p. 026001, Mar. 2022, doi: 10.1117/1.AP.4.2.026001.

[40] Y. Yang, J. Wu, M. Wang, Q. Wang, Q. Yu, and K. P. Chen, "Fast Demodulation of Fiber Bragg Grating Wavelength from Low-Resolution Spectral Measurements Using Buneman Frequency Estimation," *Journal of Lightwave Technology*, vol. 38, no. 18, pp. 5142–5148, 2020, doi: 10.1109/JLT.2020.2998614.

[41] G. Bharathan, T. T. Fernandez, M. Ams, R. I. Woodward, D. D. Hudson, and A. Fuerbach, "Optimized laser-written ZBLAN fiber Bragg gratings with high reflectivity and low loss," *Opt Lett*, vol. 44, no. 2, 2019, doi: 10.1364/OL.44.000423.

[42] P. S. Salter, M. J. Booth, L. Huang, and F. Payne, "Aberration correction for direct laser written waveguides in a transverse geometry," *Optics Express, Vol. 24, Issue 10, pp. 10565-10574*, vol. 24, no. 10, pp. 10565–10574, May 2016, doi: 10.1364/OE.24.010565.

[43] P. S. Salter, M. J. Booth, and A. Jesacher, "Refractive index profiling of direct laser written waveguides: tomographic phase imaging," *Optical Materials Express, Vol. 3, Issue 9, pp. 1223-1232*, vol. 3, no. 9, pp. 1223–1232, Sep. 2013, doi: 10.1364/OME.3.001223.

[44] R. J. Williams, N. Jovanovic, G. D. Marshall, G. N. Smith, M. J. Steel, and M. J. Withford, "Optimizing the net reflectivity of point-by-point fiber Bragg gratings: the role of scattering loss," *Opt Express*, vol. 20, no. 12, p. 13451, 2012, doi: 10.1364/oe.20.013451.

[45] G. D. Marshall, R. J. Williams, N. Jovanovic, M. J. Steel, and M. J. Withford, "Point-by-point written fiber-Bragg gratings and their application in complex grating designs," *Opt Express*, vol. 18, no. 19, p. 19844, 2010, doi: 10.1364/oe.18.019844.